


Birdlike broadband neuromorphic visual sensor arrays for fusion imaging

Received: 4 April 2024

Accepted: 11 September 2024

Published online: 27 September 2024

 Check for updates

Pengshan Xie^{1,6}, Yunchao Xu^{2,3,6}, Jingwen Wang^{2,3,6}, Dengji Li¹, Yuxuan Zhang¹, Zixin Zeng¹, Boxiang Gao¹, Quan Quan¹, Bowen Li¹, You Meng^{1,4}, Weijun Wang¹, Yezhan Li¹, Yan Yan¹, Yi Shen¹, Jia Sun^{1,2,3} ✉ & Johnny C. Ho^{1,4,5} ✉

Wearable visual bionic devices, fueled by advancements in artificial intelligence, are making remarkable progress. However, traditional silicon vision chips often grapple with high energy losses and challenges in emulating complex biological behaviors. In this study, we constructed a van der Waals P3HT/GaAs nanowires P-N junction by carefully directing the arrangement of organic molecules. Combined with a Schottky junction, this facilitated multifaceted birdlike visual enhancement, including broadband non-volatile storage, low-light perception, and a near-zero power consumption operating mode in both individual devices and 5×5 arrays on arbitrary substrates. Specifically, we realized over 5 bits of in-memory sensing and computing with both negative and positive photoconductivity. When paired with two imaging modes (visible and UV), our reservoir computing system demonstrated up to 94% accuracy for color recognition. It achieved motion and UV grayscale information extraction (displayed with sunscreen), leading to fusion visual imaging. This work provides a promising co-design of material and device for a broadband and highly biomimetic optoelectronic neuromorphic system.

Machine vision is crucial in time-sensitive scenarios, specifically in applications requiring instantaneous identification and categorization of objects, as demanded in autonomous driving and robotics. For image processing and real-time applications, visual enhancement can significantly augment machine vision's recognition and processing capabilities¹. In biological vision, birds have always been a standout presence in nature and have attracted significant interest in bionics. Enhancement of device perception through bionics of animals is an effective way to achieve more powerful neuromorphic sensing. In fact, visual enhancement, with its primary goal of improving visual perception, focuses on enhancing image features such as contrast, brightness, and color, thereby facilitating easier recognition and understanding^{2,3}. When combined with fusion imaging technology, a

single device can sense, integrate, and compute multiple signals from different sources, displaying them in a single image or video. However, vision architecture nowadays comprises distinct components for sensors, memory, and processing units. In this setup, transferring vast volumes of unprocessed data across the entire signal chain presents significant challenges, including increased energy consumption, time lags, and elevated hardware costs.

As sensors continue to evolve, boasting higher frame rates and pixel densities, they generate enormous amounts of unprocessed data at sensory terminals⁴. This evolution necessitates efficient and low-power image processing directly at the sensory terminals to handle this raw and disorganized data. The landscape of in-memory computing techniques, which unify memory and computing modules, has seen

¹Department of Materials Science and Engineering, City University of Hong Kong, Hong Kong, China. ²Hunan Key Laboratory for Super-microstructure and Ultrafast Process, School of Physics, Central South University, Changsha, Hunan, China. ³State Key Laboratory of Transducer Technology, Shanghai Institute of Microsystem and Information Technology, Shanghai, China. ⁴State Key Laboratory of Terahertz and Millimeter Waves, City University of Hong Kong, Hong Kong, China. ⁵Institute for Materials Chemistry and Engineering, Kyushu University, Fukuoka, Japan. ⁶These authors contributed equally: Pengshan Xie, Yunchao Xu, Jingwen Wang. ✉e-mail: jiasun@csu.edu.cn; johnnyho@cityu.edu.hk

substantial advancements, primarily driven by the emergence of memristive materials⁵. Simultaneously, there has been extensive exploration of in-sensor computing techniques, which strive to integrate sensing and computational capabilities within a single module⁶. As brain-computer interfaces, which connect intelligent devices to living organisms, continue to evolve, integrating in-memory computing sensors with living systems becomes a promising prospect. Organic materials are particularly well-suited for this purpose due to their mechanical flexibility, biocompatibility, and variety⁷. However, using organic semiconductors for broadband in-memory sensing and computing optoelectronic synapses still poses considerable challenges, given that individual organic materials often only provide channels for fast carrier transport and lack the means for trapping and retaining⁸.

Considerable efforts have been invested in emulating the functions of the human retina and developing an in-memory sensing and computing framework using organic materials^{9–11}. For instance, Chen introduced an organic electrochemical optoelectronic synapse that integrated a photoactive layer with donor-acceptor bulk-heterojunction interfaces into organic electrochemical transistors¹². This device exhibited significant photocurrent at low voltages, enabling high-density, non-volatile conductance states for neuromorphic computing. Its non-volatile current responded to light intensity and wavelength across the visible spectrum, facilitating the perception and memorization of various visual information. Similarly, Huang's group proposed a material-algorithm co-design featuring a light-responsive semiconducting polymer with efficient exciton dissociation and through-space charge-transport properties¹³. Their three-terminal transistor-based neuromorphic device demonstrated in-situ sensing, memorization, and pre-processing of optical inputs, including contrast enhancement and noise reduction. The device harnessed synergies between exciton dissociation, photo-gating effects, and through-space charge-transport characteristics, resulting in a dynamic reservoir computing (RC) system suitable for various tasks.

Moreover, Liu and his colleagues showcased a semi-crystalline macromolecule designed as a switching matrix for ion-based organic memristive devices¹⁴. Incorporating oxygen-rich segments with a rigid furan ring offered molecular crystallinity for thin film formation, while a small proportion of flexible ϵ -caprolactone enhanced solution processability and mechanical flexibility. These features facilitated metal cation migration, serving as the operational basis for artificial synapses. Nevertheless, optoelectronic artificial visual devices based on such material systems either lack non-volatile properties or do not respond to a broad enough range of wavelengths from solar-blind to near-infrared (NIR) to enable broadband in-memory sensing and computing processes. Furthermore, the challenge of avoiding complex transfer processes and achieving large-scale preparation and integration of various 2D materials-based devices remains an urgent issue to be addressed.

In this study, we propose a dual-junctional enhanced birdlike broadband neuromorphic visual sensor (BBNVS) array with response bands ranging from solar-blind to NIR. Birds, as born hunters in the sky, have a visual perception system unrivaled in nature. Here, in order to mimic functional components of the avian visual system that differ from human beings, the type-II Van der Waals (vdWs) heterojunction and Schottky junction were introduced. Specifically, a self-assembled poly(3-hexylthiophene-2,5-diyl) (P3HT) organic film with ordered edge-on stacking was transferred onto one-dimensional GaAs nanowires (NWs) arrays to construct P-N junction in the out-of-plane direction. Then, the Ag source and drain electrodes were applied to implement the Schottky junction. Two functional structures effectively realize the capabilities of four cone cells, rod cells, bipolar cells, and oil droplets in an avian visual system. Due to the meticulously ordered structure of the self-assembled P3HT molecule, combined with Schottky barriers, the BBNVS exhibited remarkable broadband in-memory sensing and computing performance. They achieved a capacity of over 5 bits in-memory sensing and computing processes in

blue light and green light wavelengths. Additionally, the neuromorphic visual sensor demonstrated the capability of exceeding 128 memory states within the solar-blind range. Persistent negative photoconductivity (NPC) with over 42 memory states was also realized under negative gate voltage modulation. In nature, predators would go into “energy-saving mode” when food is scarce to maintain perception of the surrounding environment. Therefore, the visual enhancement is reflected not only in the non-volatile broadband response but also in perception ability at low-power consumption. The proposed BBNVS mimicked avian visual behaviors under zero gate and source-drain voltage. In this self-power mode of operation, the power consumption of the synaptic device is nearly zero.

To cater to the future of wearables, the neuromorphic visual sensor array can be fabricated on various substrates, including glass, polyethylene terephthalate (PET), polydimethylsiloxane (PDMS), polyimide (PI), and acrylic plate. The excellent bending resistance of the chain polymers and the stress release of the nano-sized NWs at the bending interface ensures the device's superior bending resistance on different flexible substrates, even when under folding. Finally, a multi-tasking RC system was utilized to achieve multi-modal recognition of moving objects, including shape, motion, color, and UV grayscale information. The system demonstrated up to 94% accuracy for color recognition. Moreover, the BBNVS combined with the RC system completed the identification of images from UV and visible light cameras with broadband sensory enhancement, leading to UV-visible fusion imaging by integrating multidimensional information. Our approach using interior dynamic characteristics of the device reduces the redundancy of the array design and optimizes the complexity of the matrix. This work presents a promising material synthesis and co-design strategy for broadband non-volatile sensing, wearable, and highly efficient optoelectronic neuromorphic systems with multi-task in-memory sensing and computing capability.

Results

Design of the dual-junctional optoelectronic visual sensor array

Visual perception bands are not identical for different animals in nature, and birds have a top-of-the-line visual system. Among them, the kingfisher, a bird that feeds on fish and shrimp, has a wide range of visual perception (Fig. 1a). The visual perception, also known as the primary means of sensing signals, involves complex physiological and cognitive mechanisms¹⁵. Visual sensing begins when light from the environment enters the eye through the cornea (shown in Fig. 1bi). The retina contains photoreceptor cells called rods and cones, which can convert light energy into electrical signals that the brain can process¹⁶. These necessary photoreceptors are responsible for vision in dim light conditions (rods), color vision, and visual acuity in bright light conditions (cones). Unlike humans, birds have four types of cone cells that allow them to perceive red, green, and blue (RGB) as well as ultraviolet light (Fig. 1bii). Moreover, birds have brightly colored oil droplets in their optic cones that filter light entering the cells and increase sensitivity to specific wavelengths of light¹⁷. Depending on the color of the oil droplets, the effects on different wavelengths of light vary¹⁸. Once the photoreceptor cells convert the light into electrical signals, these signals are transmitted via the optic nerve to the brain. During the entire transmission process, the bipolar cell, situated between photoreceptor cells (rods and cones) and ganglion cells, plays a critical role in shaping and refining visual signals before they are transmitted to the brain, contributing to various aspects of visual processing, such as contrast enhancement, spatial filtering, and signal amplification¹⁹.

The GaAs NWs used in this work were synthesized via the two-step catalytic solid-source chemical vapor deposition (CVD) method reported before²⁰. Once the NW growth finished, scanning electron microscopy (SEM) was first performed on the obtained NWs (Supplementary Fig. 1). Then, the dry transfer technique was applied to prepare large-scale NW arrays (Supplementary Fig. 2). After that, for

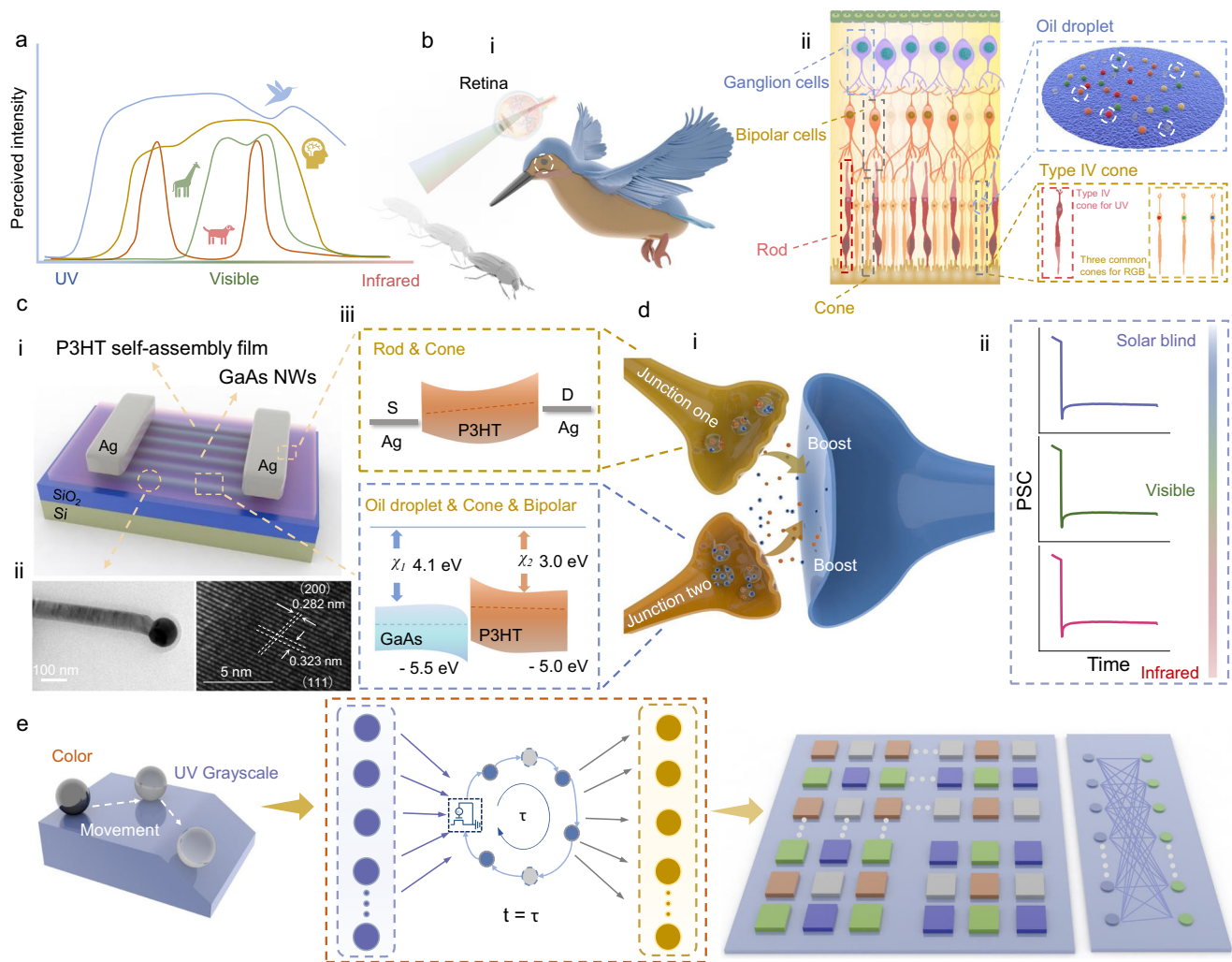


Fig. 1 | Neuromorphic visual systems inspired by avian vision. **a** Light perception range of different creatures, including dogs, kingfishers, giraffes and humans. **b–i** The process of bird visual perception. **ii** Corresponding optic nerve cell composition. **c–i** Schematic of the device structure. **ii** HRTEM of the GaAs NWs, and **iii**, energy band structure of the two heterojunctions. **d–i** Schematic illustrations of the

enhanced postsynaptic membrane potential changes and birdlike optic nerve bionics structure by two biological synapses. **ii**, Broadband non-volatile optical memory. **e**, Illustration of the optical task recognition. The input to the photo-receptor is an image of a moving ball with color information, which is processed by a construction-based all-pixel matrix.

organic semiconductor preparation, the P3HT molecules at the air/water interface can be effectively self-assembled into an ordered structure through intermolecular interactions, such as π - π stacking and hydrophobic interaction (Supplementary Fig. 3). Similar to other solution process based self-assembly methods, the thickness of the target film can be carefully controlled by adjusting the concentration or volume of the solution^{21,22}. The cross-section of SEM images with different thickness films and corresponding volume-thickness relationships at the same concentration were shown in Supplementary Figs. 4 and 5, respectively. Notably, as verified by the atomic force microscopy (AFM) and SEM, the 65 nm thick self-assembled P3HT film has flat surface (Supplementary Figs. 6 and 7, root mean square roughness = 5.37 nm) without any pinholes. Moreover, the Raman spectrum was applied to confirm the uniformity of large-area films²³. As shown in Supplementary Fig. 8, 42 random points on self-assembled P3HT/glass were selected and tested for the Raman peaks (excitation source 532 nm). Two distinct and stable peaks indicate high consistency in the self-assembled P3HT films. Raman mapping of different regions also shows a high degree of homogeneity of the film (integration wavenumber was 1450 cm^{-1}) (Supplementary Fig. 9). The corresponding device arrays and performance are shown in Supplementary Fig. 10. Following the physical transfer, the self-assembled

P3HT film was delicately placed on the NW arrays to configure the back-gate geometry, as shown in the device schematic (Fig. 1ci). The Raman spectroscopy was also applied and confirmed the vdWs contact between the organic film and NWs array with negligible peak shift (Supplementary Fig. 11)^{24,25}. To further evaluate the crystallinity and the growth orientation of GaAs NWs, high-resolution transmission electron microscopy (HRTEM) was carried out as displayed in Fig. 1cii and Supplementary Fig. 12. The energy dispersive X-ray spectroscopy (EDS) mappings were as well performed on the GaAs NW, where the elements of Ga and As were all distributed in a uniform manner along both axial and radial directions of the NW (Supplementary Fig. 13). The required performance test of NW arrays was carried out (Supplementary Fig. 14). The NW arrays were prepared on Si/SiO₂ substrate by the dry contact printing method. Photolithography was utilized to define the channel region with a length of 2 μm , and Ni was used as source/drain (S/D) metal contact electrodes (Supplementary Fig. 14c, d). Then, 25 randomly selected devices were characterized. They all worked stably and demonstrated the transfer characteristics of an N-type semiconductor (Supplementary Fig. 14e), which is consistent with our previous results²⁰. For dual-junctional optoelectronic synapse, the band structure of the Schottky junction and P-N junction are shown in Fig. 1cii^{26,27}. Here, two distinct junctions play the role of two axon

terminals jointly releasing neurotransmitters to enhance the post-synaptic membrane potential changes (Fig. 1di). Meanwhile, the two heterojunctions also mimic the functions of the four cone cells, oil droplets, bipolar cells, and rod cells in avian vision, respectively. Due to this synergy, bionic vision enhancement is enabled, including broadband response, multi-state in-memory computing with positive photoconductivity (PPC) and NPC, and near-zero ultra-low power consumption (Fig. 1dii). Drawing inspiration from bio-sensory systems, RC systems, different from various artificial neural network models, with only the readout function requiring training, can effectively compute complex time-related data at a low training cost (Fig. 1e)²⁸. Combined with the broadband neuromorphic visual sensor of kingfisher-like vision, it can effectively recognize multi-dimensional information such as color, motion, and UV grayscale of moving objects.

Optoelectronic behaviors of neuromorphic sensors on arbitrary substrates

Although P3HT has been widely used as a semiconductor material in various optoelectronic devices, its narrow absorption band and typical optoelectronic device performance have hindered its further application^{29,30}. Supplementary Fig. 15 demonstrates the absorption range of the self-assembled P3HT film. In order to overcome this “visual deficit”, the BBNVS was constructed to realize kingfisher-like broadband in-memory sensing and computing. Specifically, visual enhancement here is manifested in various ways: (1) enhanced sensing range and capabilities, including wider response bands and the ability to detect weak signals; (2) non-volatile optical signal storage capability; (3) ultra-low power consumption operating modes. Supplementary Fig. 16a–c show the typical synaptic plasticity of excitatory postsynaptic current (EPSC) for the optoelectronic synapse with different response bands and optical power densities. In this case, the light pulse and the S/D current were regarded as the presynaptic input and postsynaptic signal, respectively. Notably, a 0.5 s laser pulse leads to a long-term memory effect for optical signal, significantly different from devices with only P3HT film (Supplementary Figs. 17 and 18). Moreover, efficient separation and injection of photogenerated carriers at the P–N junction interface effectively enhances the photocurrent of the device (over 6 times), further enhancing the perception of the artificial visual system in dim light environments^{31,32}. When the metal-semiconductor contact is closer to ohmic contact, the P3HT film displays photodetector-like properties with 0.1 Hz light frequency³³. The details of the working mechanism of the dual junctions will be explained later. Moreover, 100 consecutive presynaptic light spikes (1.5 Hz) with different wavelengths were applied to induce the linear increase of the EPSC, demonstrating linear weight update with optical inputs (Fig. 2a–c). Also, the non-volatile storage behaviors were realized in different bands. In particular, as shown in the enlarged detail view, each light pulse input results in a stable, amplitude-consistent increase and uniform steps in neural weights. These linear in-memory sensing and computing behaviors help simplify the design and optimization process of neural networks and enhance the stability and reliability of devices³⁴. It is noted that excellent non-volatile optical signal storage is realized not only in the visible range but also in the solar-blind wavelength (Supplementary Fig. 19). Continuous light pulses (261 nm, 0.32 mW cm^{−2}, 1 Hz) were also applied to result in linear changes in postsynaptic synaptic weights and surpassing 128 memory states (Supplementary Fig. 20). GaAs is a classical material for infrared detection, especially in the near-infrared and short-wave infrared bands³⁵. The vdWs P–N heterojunction empowers P3HT channel detectable capability in the infrared band. The infrared laser-excited photogenerated electron-hole pairs in GaAs NWs would be separated at the interface by the built-in electric field, and holes would be injected into the P3HT channel to form a photocurrent (Supplementary Fig. 21).

In achieving specific response and contrast enhancement, bipolar cells play a key role in shaping and refining visual signals before they are

transmitted to the brain. This contribution includes a range of visual processing functions, including contrast enhancement, spatial filtering, and signal amplification. Therefore, mimicking and realizing the role of bipolar cells in the visual system is essential for achieving visual enhancement. At longer pulse intervals (10.5 s), the BBNVS demonstrates over 5 bits in-memory sensing and computing process in the blue (450 nm), green light (532 nm) range (Fig. 2d and Supplementary Fig. 22a) and 4 bits in the red light (635 nm) range (Supplementary Fig. 22b). Moreover, the device also demonstrated the ability to code 4-bit spatiotemporal information (Supplementary Fig. 23). Meanwhile, when negative gate voltage was applied on gate electrode ($V_G = -5$ V), NPC was realized in the P3HT channel to mimic the function of a bipolar cell. Over 5 bits of in-memory sensing and computing process with inhibitory postsynaptic potential was induced by 450 nm light pulses with 10.5 s intervals (Fig. 2e). Supplementary Fig. 24 illustrates the working process of the device under varying V_G modulation. When $V_G = 0$ V and a light pulse is applied to the device, electron-hole pairs separate at the interface and are transported due to the influence of the energy bands (Supplementary Fig. 24a, b). Consequently, electrons in the NWs generate a continuous photo-gating effect, maintaining the carrier concentration in the P3HT channel. When a negative V_G is applied to the gate, the P3HT channel, being a P-type semiconductor, is already open, leading to a substantial accumulation of holes at the interface due to the negative gate voltage (Supplementary Fig. 24c). Capacitive coupling occurs at the P3HT and NW interface under V_G modulation. Figure 2d, e also depict the different dark currents under two distinct V_G conditions. When light pulses are applied (Supplementary Fig. 24d), the electric fields impede the transport of photogenerated electrons and holes. Within the two semiconductors, photogenerated electrons and holes rapidly recombine. Additionally, photogenerated holes in the NWs induce further carrier scattering in the P3HT channel. This leads to NPC, characterized by reduced channel holes due to interfacial scattering^{36,37}. Furthermore, electrical pulses were utilized to investigate the reduction in channel current resulting from hole scattering at the interface. The electrical stimuli of varying intensities with a duration of 0.1 s were applied to the gate electrode (Supplementary Fig. 25). The channel current first shows an increasing spike. Then, it decreases rapidly at the end of the pulse duration. Moreover, the magnitude of the current reduction is positively correlated with the pulse intensity, implying that more holes are generated at the channel interface and increasing the probability of trapping. After that, interface-captured holes would cause stronger carrier scattering at the end of the pulse, thereby reducing the channel current. Interestingly, the 261 nm stimulus can also successfully achieve PPC and NPC (Supplementary Fig. 26). Therefore, higher photon energies and greater penetration with short wavelength bands allow a large number of photogenerated carriers to be induced inside the two semiconductors, which could recombine with existing carriers and produce interfacial scattering.

With the explosion of artificial intelligence (AI), wearables are in the fast lane. An endless variety of products have been rapidly entering human life and trying to change the modern lifestyle, such as brain-computer interfaces, virtual reality (VR) and augmented reality (AR) devices, and all kinds of human-computer interaction devices³⁸. Superior bending resistance, or flexibility, is an important metric in developing wearable devices. Flexible devices can increase the applicability of wearable devices and expand their application potential. From smart sensors to human health detection, flexible wearable devices have shown great market prospects with the support of AI technology. Due to physical transfer and large-area self-assembly preparation methods, the optoelectronic synapse can achieve high-performance in-memory sensing and computing processes on arbitrary substrates with excellent bending resistance performance. The self-assembled P3HT film can be physically transferred to various substrates with the size of 2.5 × 2.5 cm, including glass, acrylic plate, PET, PDMS, PI, and so on (Supplementary Fig. 27). The following AFM images reveal the

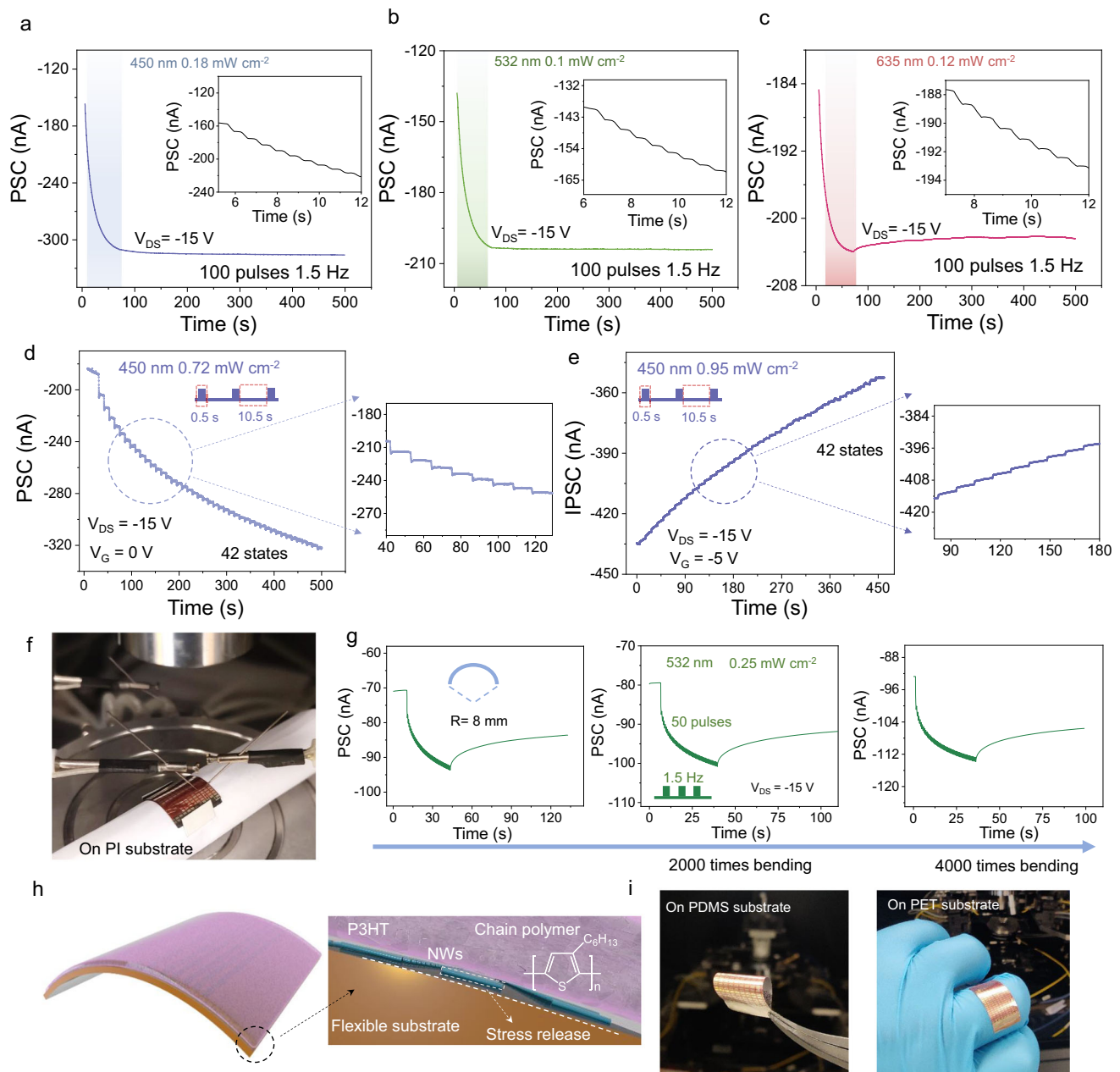


Fig. 2 | Optoelectronic and flexible properties of the dual-junction enhanced birdlike broadband neuromorphic visual sensor (BBNVS) array on different substrates. Long-term plasticity of the synaptic devices with (a), 450 nm (b), 532 nm, and (c), 635 nm 100 consecutive presynaptic light spikes (1.5 Hz). **d** Over 5 bits PPC in-memory sensing and computing process states realized with the 450 nm pulses (10.5 s intervals). The figure on the right is a zoomed-in detail of the weight changes. **e** Over 5 bits NPC in-memory sensing and computing process states realized with the

450 nm pulses (10.5 s intervals) when $V_G = -5$ V. The figure on the right is an enlarged detail of the weight changes. **f** Photograph of the testing under bending situation. **g** Long-term plasticity of the synaptic devices after bending 4000 times with a bending radius of 8 mm. **h** Schematic of the stress relief of NWs at the substrate interface. **i** Photograph of the synaptic device array on PDMS and PET substrates. The inner figures are the long-term plasticity with 50 consecutive 532 nm pulses (1.5 Hz, 0.25 mW cm^{-2}).

denseness and continuity of the P3HT films on different substrates (Supplementary Fig. 28). Supplementary Fig. 29a–c show the long-term plasticity characteristics in the visible range with the device's structure of PI/GaAs NWs/P3HT/Ag. The synaptic weight could be effectively modulated by several light pulses and different power densities. It is noted that this two-terminal device can also be capable of effective optical signal storage. In the field of wearables, our artificial synapses also have the potential to be wearable in-memory sensing and computing optoelectronic neuromorphic visual sensory arrays. Therefore, the bending stability of the device is one of the important metrics to be considered. Figure 2f demonstrates the bending testing process of the

devices on the PI substrate. After the device was bent 4000 times with a bending radius of 8 mm, the device still had almost constant weight changes to continuous optical stimuli of 532 nm (Fig. 2g). The corresponding test of 1000 to 4000 bends is shown in Supplementary Fig. 30. As the number of bends increases, the dark current of the device increases slightly, which can be attributed to film deformation and degradation of the contact interface of P–N junction and Schottky junction. We believe that the excellent bending resistance of the synaptic device is mainly due to three reasons: P3HT is a chain polymer semiconductor, the relatively small size of the NWs and vdWs contact. Firstly, P3HT has been widely used in stretchable, wearable, and flexible

devices^{39,40}. We also prepared the self-assembled P3HT films on a PDMS substrate. The entire film can withstand all kinds of deformation, such as stretching, twisting, and poking (Supplementary Fig. 31). As shown in Fig. 2h, when smaller NWs are located on a large flexible substrate and bent together, the bending radius of the NWs will be relatively small; therefore, the stress applied will be relatively small on a single NW⁴¹. Then, the Raman spectroscopy was adopted to investigate the effect of stress on different interfaces (Supplementary Fig. 32). It is evident that this physical transfer method ensures vdWs contact between the two materials, which guarantees high film quality when additional stress is applied. The C-C and C=C stretching modes of thiophene show almost no noticeable change (Supplementary Fig. 32b)⁴². On the contrary, the spin-coating P3HT film on NWs would be significantly affected by the stress (Supplementary Fig. 32c). The C-C mode generates a significant blueshift of the peak position under stress (shift to higher wave-numbers) and full width at half maximum shows substantial degradation. In this case, stress causes changes in the dihedral angles of P3HT molecules, affecting their overall crystallinity and arrangement⁴³. This stress release at the interface, coupled with the excellent bending properties of the P3HT, provides the device with stable operation and bending resistance on arbitrary flexible substrates. Figure 2i shows the neuromorphic visual sensor array on PDMS and PET substrates, indicating our devices remain stable under the same test conditions on different substrates (Supplementary Fig. 33). In particular, when the device array is prepared on some thin and light substrates, it can be randomly pasted on the surface of skin or fabric to realize wearable integration (Supplementary Fig. 34).

Working mechanism and self-powered operation of the birdlike visual sensing

The efficacy of charge transport in conjugated polymers hinges significantly upon the degree of crystallinity and the orientation of crystallites. Therefore, in order to better study the working mechanism of the dual-junctional optoelectronic synapse, synchrotron grazing-incidence wide-angle X-ray scattering (GIWAXS) was utilized to explore the molecular arrangement of the self-assembled P3HT film (Fig. 3a, b). In general, the arrangement of P3HT molecules is divided into four types: edge-on, face-on, chain-on, and mixed-phase⁴⁴. It is evident that compared with the spin-coating method, the self-assembled P3HT film has more substantial diffraction peaks in the out-of-plane with (100) direction, which is clear evidence of edge-on lamellae distinguishable strong diffraction peaks along the z-axis. Figure 3c demonstrates a highly ordered edge-on arrangement of P3HT molecules in which the π - π stacking is extended along with in-plane direction. In this stacking way of P3HT molecules, the alkyl chains of P3HT molecules are perpendicular to the surface of the substrate, resulting in closer π - π stacking interactions between molecules. Meanwhile, the alkyl chains in P3HT mainly act as isolated molecules and do not conduct charge carriers. The π - π stacking structure provides a continuous electron transport channel, which results in a shorter transport path for carriers and facilitates their leaps and transports along specific directions^{45,46}. Therefore, the P-N vdWs heterojunction not only takes on the function of separating the carriers but also serves the capability of trapping and storing information. The transport barriers caused by alkyl chains perpendicular to the substrate make carrier recombination more difficult, contributing to the functionality of non-volatile storage (Fig. 3d). In this case, a flawless interfacial and organically ordered arrangement of the organic film is crucial. Compared to the self-assembled film, P3HT films prepared by the spin-coating method prefer a mixed phase, including face-on, edge-on, and other mixed arrangements. Spin-coating P3HT film on NW arrays also introduces surface roughness, leading to increased hole formation. Establishing long-range ordered π - π conjugate bonds (transport channels) is hindered, raising the carrier transport barrier⁴⁵. Meanwhile, the alkyl chain cannot be arranged in an orderly out-of-

plane direction, which will further reduce the barrier of carrier recombination and the storage time (Supplementary Fig. 35). Besides, we investigated the effect of NWs alignment on device performance. As illustrated in Supplementary Fig. 36, the two devices feature arrays of NWs aligned perpendicular and parallel to the channel, respectively. When the NWs are oriented perpendicular to the channel, the device exhibits marginally reduced transistor performance but enhanced optical signal storage capability. In the BBNVS device structure, NWs do not directly contribute to channel conduction. Therefore, we believe that if the NWs are perpendicular to the direction of carrier transport in the P3HT film, it may hinder the recombination of trapped photogenerated carriers with the P3HT film. Consequently, this orientation promotes a more substantial photo-gating effect and enhances photocurrent storage performance.

For another junction (Schottky junction), based on the differential charge density (Fig. 3e), electrons move from P3HT to Ag due to the work function difference between them. This directional electron transfer brings about upward band bending of P3HT near the interface (Fig. 3f), and the barrier at the metal-semiconductor interface similarly enhances carrier retention inside the P3HT channel⁴⁷. The I-V curves of the synaptic devices demonstrate the existence of a Schottky barrier (Supplementary Fig. 37). The apparent current asymmetry (rectification effect) confirms the presence of Schottky barriers due to Ag electrodes. In this case, the P3HT channel has built-in electric fields in both in-plane and out-of-plane directions, which vertically distributed P-N heterojunctions can effectively separate carriers, and parallel Schottky junctions can induce carrier movement. The transfer characteristic curves of the three-terminal devices before and after light irradiation further demonstrate the advantages of broadband optical signal storage (Supplementary Fig. 38). After irradiation by solar-blind and visible light, respectively, the threshold voltage (V_{th}) and photocurrent of the devices are significantly and consistently shifted. The V_{th} can be shifted in the positive direction by more than 20 V, implying a significant increase in channel hole concentration⁴⁸. Not only that, but the optoelectronic synapse enables optical signal sensing without external energy sources. The two built-in electric fields allow carriers to be separated and transported by self-power working mode⁴⁹. The different synaptic behaviors, including EPSC, spike-number dependent plasticity, and spike-intensity dependent plasticity, were successfully mimicked under V_G and $V_{DS} = 0$ V (Supplementary Fig. 39 and Supplementary Fig. 40). Therefore, in this mode of operation (self-power), the power consumption of the synaptic device is close to zero⁵⁰. This capability to maintain weak signal perception without external energy sources mimics the self-saving energy mechanism of predators when food is scarce. Thus, the synergistic effect of the two heterojunctions jointly achieves visual perception enhancement, including non-volatile storage of broadband optical signals, effective perception in dim light environments, and near-zero power consumption operating mode.

In addition, the photoluminescence (PL) spectra and X-ray photoelectron spectroscopy (XPS) were utilized to show the carrier transfer of the P-N heterojunction, respectively. As shown in Fig. 3g, the PL mapping (532 nm laser excitation with the same power) demonstrates the clear demarcation line for P3HT films with and without GaAs NWs beneath it. The corresponding PL peaks in regions A and B also exhibit the separating process of photogenerated electron-hole pairs in this P-N heterojunction (Fig. 3h)⁵¹. Moreover, the XPS peak in Fig. 3i of S 2p would slightly shift 0.3 eV towards lower binding energy, indicating the carrier transfer happened into the organic molecule-nanowire heterojunction⁵². The human visual system relies on millions of nerve fibers to convey data to the brain for processing. Consequently, in the development of artificial visual systems, it is imperative that devices possess integrable and arrayable characteristics to enable seamless fabrication processes. In this work, we fabricate a 5×5 array to realize optical signal storage of the image. A 1 s 450 nm pulse was applied to the synaptic device array through a

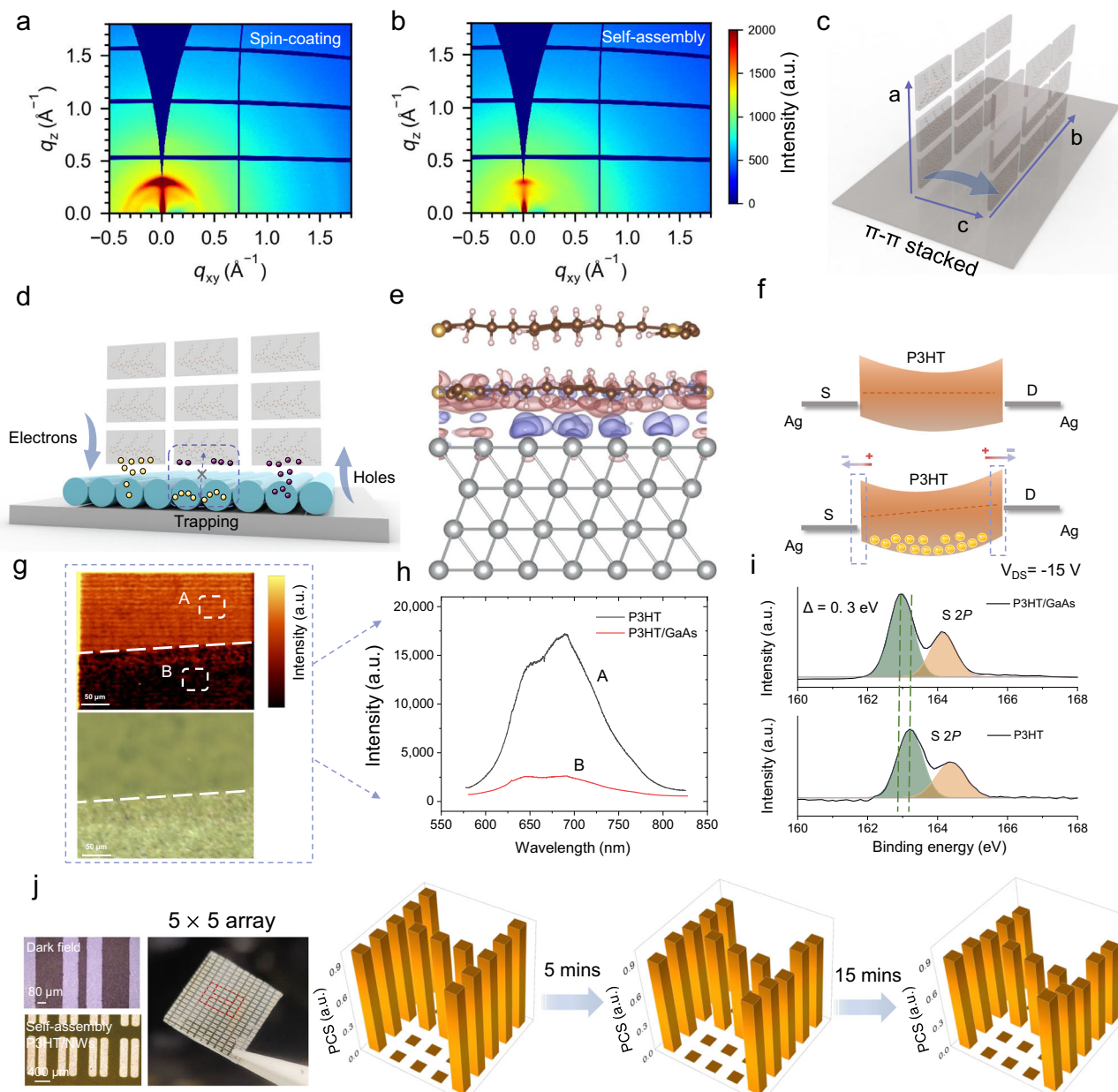


Fig. 3 | Design strategy and working mechanism of the birdlike broadband neuromorphic visual sensor. Synchrotron GIWAXS of (a), the spin-coated and (b), self-assembled P3HT films. c Schematic of the ordered edge-on arrangement of P3HT molecules in which the π - π stacking is extended along with in-plane direction. d Schematic of the interface of P3HT/GaAs NWs and the carrier transportation. e Charge transfer at the interface of P3HT/Ag simulated by VASP. f Schematic of the retention of channel carriers by Schottky barriers. g PL mapping of the P3HT/GaAs

NWs heterojunction, where region A is only the P3HT film, and region B is the P3HT film with nanowire arrays beneath it. h PL peaks in the corresponding region. i XPS peaks of the P3HT films with and without GaAs NWs beneath it. j A 5 × 5 array to realize optical signal storage of the image. The synaptic device array exhibits stable, non-volatile storage upon receiving an optical signal stimulus, and the H-shape feature is still well preserved after 1000 s.

H-shaped shadow mask, and the percentage change of the current is shown in Fig. 3j. The synaptic device array exhibits stable, non-volatile storage upon receiving an optical signal stimulus, and the shape of the graphic is still well preserved after 1000 s. Supplementary Fig. 41 demonstrates the EPSC of the device array after single light pulse irradiation. The stable operation of the array reflects the homogeneity of the devices and the potential utilization for large-area preparation.

Multi-tasking RC and fusion imaging

Drawing inspiration from bio-sensory systems, RC systems, among various artificial neural network models, leverage dynamic reservoirs endowed with short-term memory to map temporal input features into

a high-dimensional feature space. The readout function layer efficiently analyzes the projected features for classification and time series analysis tasks. With only the readout function requiring training, the system can effectively compute complex time-related data at a low training cost¹³. Figure 4a illustrates the schematic of the RC system for motion color recognition. A small red ball with a specific pattern painted on its surface with sunscreen served as the identification object. Its movement, color, and UV graphic information can be recognized by the RC system. In particular, as human visual perception, the general range of perception is concentrated in the visible light band. Also, our device effectively enhances the range of its perception and realizes the recognition of UV information. Moreover, 24 Hz would

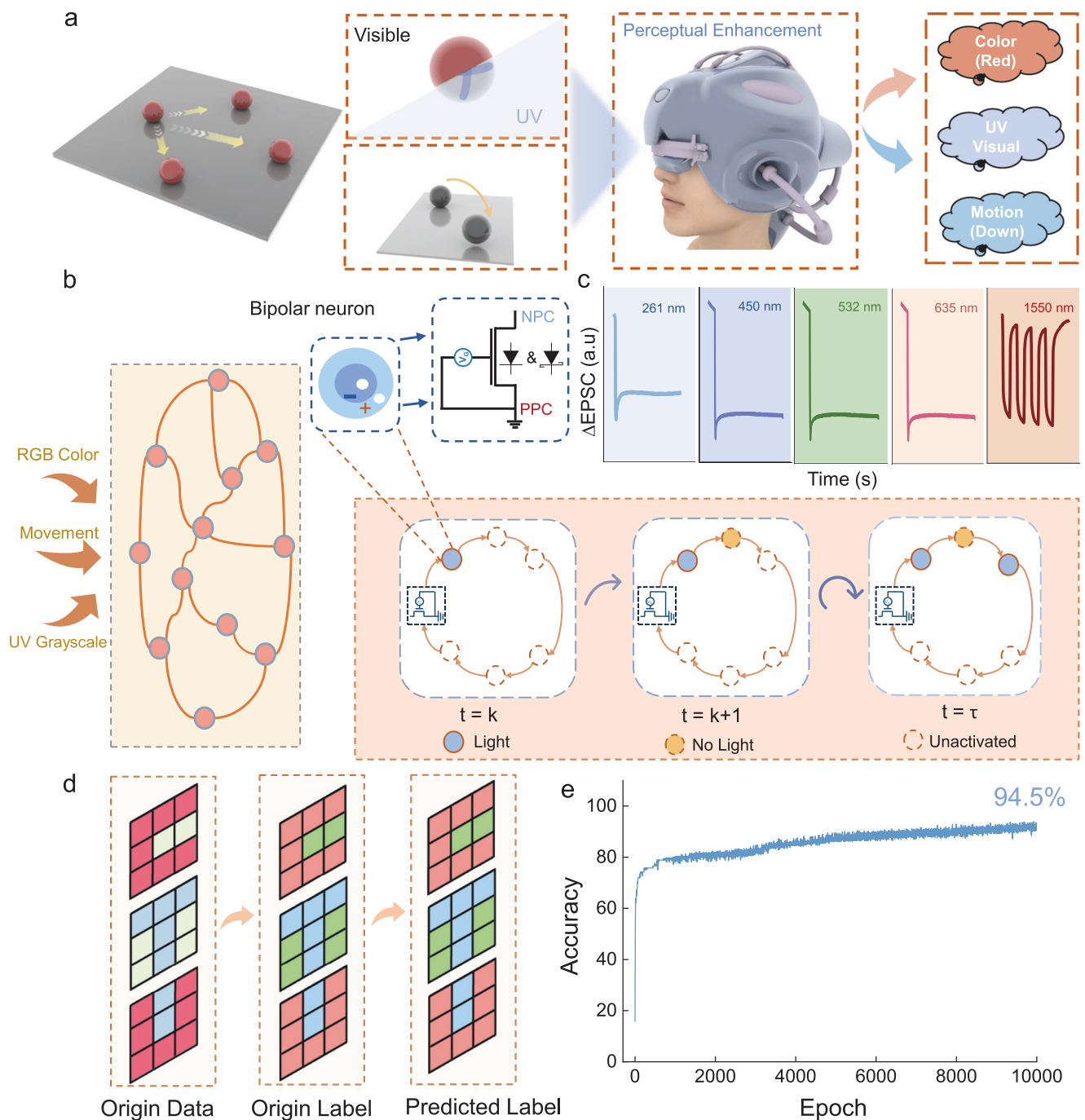


Fig. 4 | Multi-task in-memory sensing and computing capability with RC.

a Illustrative diagram of a multifunctional bionic vision system. Combining bird-like vision, which can detect ultraviolet light, with human vision can lead to the realization of a bionic vision system that integrates multiple types of information.

b Illustration of dynamic RC system. **c** EPSC characteristics under different wavelengths of light. **d** Different color combinations of 'C', 'T', 'U' based on self-built color datasets and their visualizing labels and visualizing predicted labels. **e** Classification accuracy of color recognition during training epochs.

be considered a cut-off point for general visual recognition, also widely used in cinematography. Therefore, the BBNVS also demonstrated the response with high-frequency input signal to show the potential for moving object perception (Supplementary Fig. 42). It is similar to endowing the UV recognition ability of birds to human visual perception, thereby achieving visual enhancement. Specifically, Fig. 4b depicts the schematic diagram of the dynamic RC system. Initially, various information from the image is pre-processed and converted into a series of light pulses by the algorithm. Each input signal frame generates a pulse string with a total length of τ and a pulse width of δ (e.g., [101101]). During input at time $t = k$, the pulse string illuminates

the node at position 1. At time $t = k + 1$, the pulse string at the corresponding position is 0, indicating no light is applied to a single node⁵³. This process continues until time $t = \tau$, with the device's response state inherited from the previous moment. The BBNVS can simulate the sensitivity of human eye cone cells to different wavelengths of color light, exhibiting varying light-induced responses under RGB illumination (excitation wavelengths of 635 nm (R), 532 nm (G), and 450 nm (B), respectively)⁵⁴. Not only that, but the visual enhancement extends the device's perceptual range considerably (from solar-blind 261 nm to infrared 1550 nm), which endows the device with greater bionic functionality to mimic other organisms in the natural world, such as birds

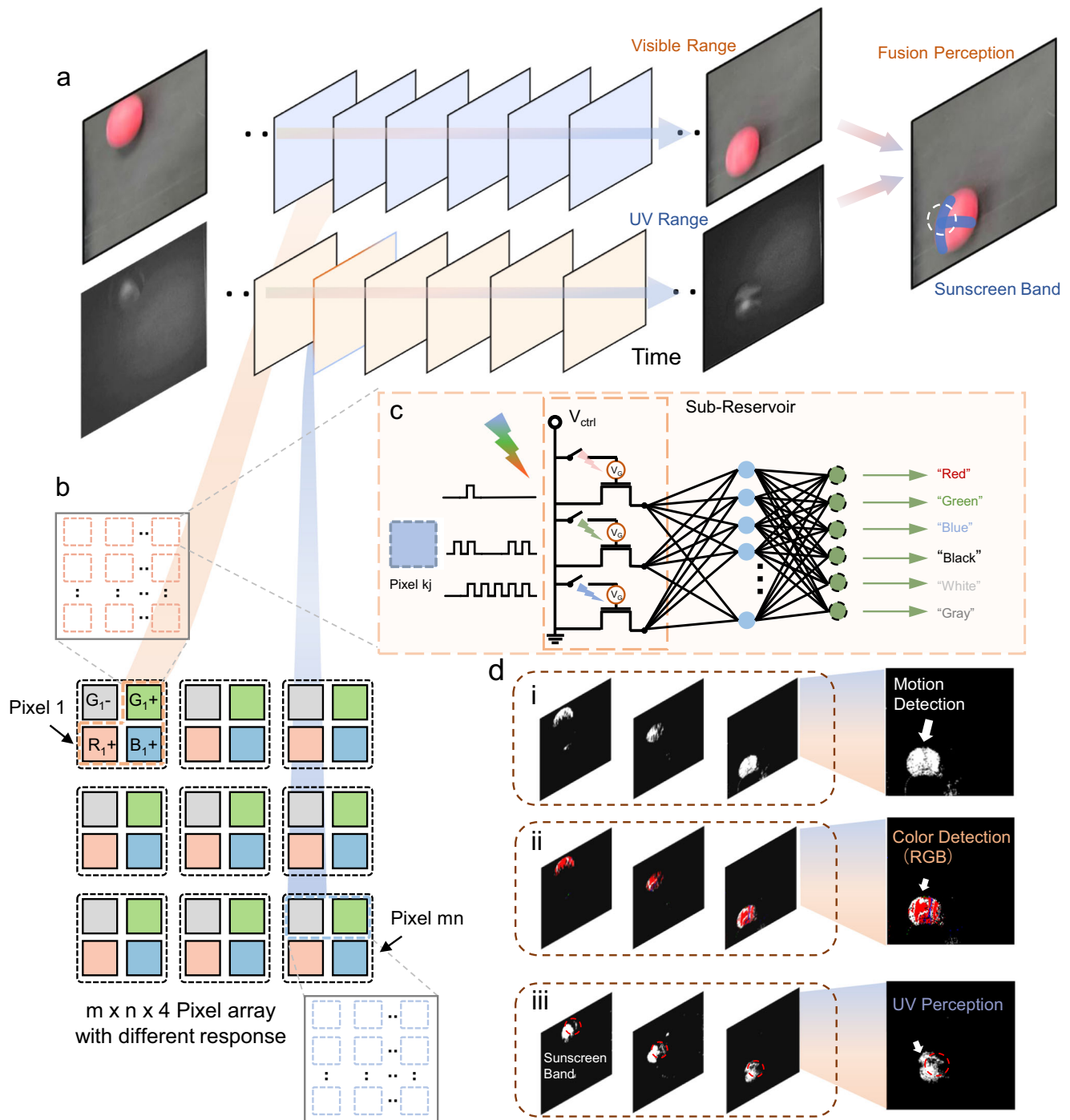


Fig. 5 | Fusion visual imaging based on a BBNVS-based RC system. **a** An example of a moving red ball patterned with transparent sunscreen. It is used to demonstrate the effect of hybrid recognition. **b** Total pixel matrix constructed and the two

sub-pixel matrices constituting it. **c** Illustration of the sub-reservoir circuit used for motion detection. **d-i** Motion, and (ii), color recognition results in normal view and the motion detection results in (iii), UV view.

(Fig. 4c). Subsequently, we verified the effectiveness of the reservoir for color recognition. Initially, we established a small color dataset and validated it with different color combinations of 'C', 'T', and 'U' (Fig. 4d). It is shown in Fig. 4d that the visualized original data, original labels, and predicted labels after the RC system of these three letters. Taking the "green" label as an example, assuming the RGB format of any pixel is [0, 255, 0], and its corresponding label is 0. During the visualization process, the label 0 is replaced by [138, 232, 125] to represent the data labels and prediction results. The RC system based on BBNVS demonstrated up to 94% accuracy for color recognition, as depicted in Fig. 4e. Detailed procedures and methods for color

recognition can be found in Supplementary Fig. 43 and Supplementary Method 1.

Furthermore, the optoelectronic synapse-based RC system successfully achieves multi-information recognition and fusion vision imaging by constructing an array of total pixel reservoirs. We presented an example of a moving red ball patterned with transparent sunscreen (Fig. 5a). Firstly, a red ball was coated with transparent sunscreen, which was invisible to the naked eye with the shape of a cross. In this case, this moving red ball carries multiple dimensions of information, shape, position, color, and sunscreen graphics (grayscale), a typical multi-task recognition with higher recognition

difficulty. Then, this example contains a normal camera view (visible range) and a UV camera view, respectively. The input at each moment is preprocessed and converted into light pulses fed into the reservoir matrix. We take two of the adjoining frames as an example of their preprocessing and show their diagrams in the spatiotemporal view and methods in Supplementary Fig. 44. In Fig. 5b, the total pixel reservoir matrix consists of $m \times n$ units and $m \times n \times 4$ subunits, where the values of m and n are related to the input image size configuration. In the total pixel reservoir array, 2 sub-reservoir pixel matrices are included⁵⁵. Each sub-reservoir pixel undertakes different tasks by outputting different currents. The blue sub-reservoir pixel matrix is used for motion detection. A schematic of each sub-reservoir circuit in this array is shown in Supplementary Fig. 45. The orange sub-reservoir pixel matrix is used for color detection³⁴. A schematic of each sub-reservoir circuit in this matrix is shown in Fig. 5c. The three devices in the orange boxed circuit diagram correspond to G_+ , R_+ , and B_+ subunits in the total pixel array reservoir in Fig. 5b (representing the positive photoconductive devices used for inputting green, red, and blue light, respectively)⁵⁶. By processing the RGB three-channel data of the input image pixels, it is converted into corresponding optical pulses of three different wavelength bands that are input into the sub-reservoir's units, respectively. The optical signal is then converted into three visual features received by the readout layer. The color is classified and recognized by two fully connected layers. For the normal camera view and the UV camera view, the multi-tasking RC system performs multidimensional perception. When a moving object is detected during the normal view, the pixels of the moving subject are converted into light pulses to be fed into the sub-reservoir array for color recognition. It can be seen that when there is motion behavior, the output displays the motion trajectory (Fig. 5di). The result of the color recognition of the moving object is depicted in Fig. 5dii, and the motion trajectory under the UV camera view is illustrated in Fig. 5diii. The result of motion detection can be modulated by applying a threshold. The comparison between our method and the previous method using different thresholds is shown in Supplementary Fig. 46 and Supplementary Method 2. It can be seen that patterns that are not visible to the naked eye can be observed under UV camera view and even perform well in the case of very low ambient brightness. Besides, our approach reduces the redundancy of the array design of the device and optimizes the complexity of the matrix. In particular, the leaner array design (half the parameter values compared with previous works) avoids complex addition or subtraction operations and accomplishes efficient visual imaging in more complex recognition scenarios. The dynamic video generated by the RC system containing UV grayscale information is presented in Supplementary Movie 1. The corresponding screenshots of the videos are displayed in Supplementary Fig. 47 (Supplementary Movie 2 and 3). Therefore, due to the enhancement of visual perception, multidimensional information, including movement, color, and grayscale, can be identified and fused for imaging on the RGB and UV band (Fig. 5a). The corresponding comparisons with related works are shown in Supplementary Table 1.

Discussion

In conclusion, we successfully constructed two heterojunctions, in-plane and out-of-plane, for the BBNVS array and fusion image. Own to the meticulous synthetic arrangement of the P3HT molecule, the vdWs P-N junction, combined with a Schottky barrier, enabled multifaceted kingfisher-like visual perception enhancement, including (1) non-volatile storage of broadband optical signals ranging from solar-blind to infrared, (2) effective perception in dim light environments and (3) a near-zero power consumption operating mode. Specifically, over 5 bits of in-memory sensing and computing process were realized by persistent PPC and NPC within the visible range. The 5×5 optical signal storage arrays further demonstrated the potential for large-area integration of synaptic devices. A unique physical transfer preparation

method endowed the synaptic device with excellent compatibility to work on arbitrary substrates, aligning it closely with the rapid development of future wearable devices. Furthermore, the RC system was applied to recognize multidimensional information. Based on the dual-junctional enhanced BBNVS, the system demonstrated up to 94% accuracy for color recognition. Notably, by recognizing moving objects in two imaging modes (visible and UV), the system identified all information of the red moving ball, including movement, color, and UV grayscale, thereby achieving fusion visual imaging of UV-visible light. Our neuromorphic visual sensor, combined with a RC system, provides a promising device design for broadband non-volatile sensing, wearable, and highly efficient photoelectric neuromorphic systems with multi-task in-memory sensing and computing capability. This combination of non-volatile internal dynamic properties can further provide broader application perspectives in the direction of leaner array design and bionic spatio-temporal information recognition.

Methods

Measurement and characterization

The optoelectronics performance of the FETs was then characterized with a standard electrical probe station and an Agilent 4155 C semiconductor analyzer (Agilent Technologies, Santa Clara, CA). The morphologies and EDS mapping of as-prepared NWs were examined using scanning electron microscopy (SEM, Quanta 450 FEG, FEI) and high-resolution transmission electron microscopy (HRTEM, Thermo Scientific, Talos F200X). The morphologies of organic films were confirmed by AFM (Bruker Dimension Icon AFM). The Raman and PL spectroscopy were applied to characterize interface contact and carrier migration (FLS980). The power was calibrated and measured for the light stimuli by a power meter (PM400, Thorlabs). The irradiation power was tuned by a modulator (AFG 2005, Good Will) connecting to the laser source. The injection of carriers was confirmed by XPS (ThermoFisher, ESCALAB 250Xi). The molecular arrangement of P3HT was investigated by synchrotron GIWAXS (Shanghai Synchrotron Radiation Facility).

Self-assembly of the P3HT film

The P3HT (purchased from Sigma-Aldrich without further purification) dissolved in toluene (10 mg mL^{-1}) is prepared in the glove box and stirred continuously at 60°C for 120 min. Subsequently, $50 \mu\text{L}$ of the polymer solution was gently dropped onto the surface of deionized water, where the polymer solution diffused rapidly due to the Marangoni effect. Therefore, A nanofilm is formed in approximately 2 min as the solvent evaporates and floats on the water surface⁵⁷. During the evaporation of toluene, the P3HT molecules at the air/water interface can be effectively self-assembled into an ordered structure through intermolecular interactions, such as π - π stacking and hydrophobic interactions.

Spin-coating of the P3HT film

The P3HT was dissolved in toluene and stirred at 60°C for 6 h to form a homogeneous solution of 10 mg mL^{-1} . The P3HT solution was spin-coated on the cleaned Si/SiO₂ substrate at 2500 rpm for 30 s, followed by annealing at 70°C for 3 h under vacuum to obtain P3HT semiconductor films.

CVD synthesis of GaAs nanowires

GaAs (99.999%, purchased from China Rare Metal without further purification) nanowires were synthesized on SiO₂/Si wafer pieces (50 nm thick thermally grown oxide) in a two-zone horizontal tube furnace using a chemical vapor transport method^{20,58}. The GaAs powder was loaded into a boron nitride crucible at the upstream zone of the furnace. The growth substrate was pre-deposited with a 5 nm thick (nominal thickness) Au film as the catalyst and was set at the downstream zone. The temperature of the downstream zone was first elevated to 800°C and kept for 10 min to anneal the Au catalyst. Then, the temperature of the downstream zone was cooled directly to the growth

temperature (640 °C) for the first step of growth, and the source temperature started to elevate simultaneously. The first nucleation step began when the source temperature reached the designated value (800 °C). After 1–2 min, the downstream was stopped with the heating and then cooled to a second-step growth temperature (570 °C). Finally, the second step, growth, lasted for 30 min. The hydrogen (99.9995%) was used as a carrier gas during the entire growth process, with the flow rate maintained at 100 sccm.

Material transfer and device preparation

The dry printing transfer method was utilized for fabricating the NWs array. The growth of donor substrate with as-grown NWs was flipped upside down and placed on the clean receiver SiO₂ substrate (n⁺⁺ Si wafer bearing 200 nm SiO₂ dielectric layer)^{59,60}. After gently moving the donor substrate in one direction, the NWs will be separated from the growth substrates and laid down on the target substrate. The preparation of large-scale nanowire arrays can be achieved by this contact printing method. After that, a large area of self-assembly P3HT film was transferred onto the GaAs NWs using simple stamping. Finally, 50 nm Ag source and drain electrodes were thermally evaporated on the semi-conducting layer through a shadow mask at a rate of 0.5 Å/s. The width and length of the channel are 1000 µm and 80 µm, respectively.

Data availability

Relevant data that support the key findings of this study are available within the article and the Supplementary Information file. All raw data generated during the current study are available from the corresponding author upon request. Source data are provided with this paper.

References

- Zhou, G. et al. Full hardware implementation of neuromorphic visual system based on multimodal optoelectronic resistive memory arrays for versatile image processing. *Nat. Commun.* **14**, 8489 (2023).
- Qiu, T. et al. Vision-driven metasurfaces for perception enhancement. *Nat. Commun.* **15**, 1631 (2024).
- Yang, Y. et al. In-sensor dynamic computing for intelligent machine vision. *Nat. Electron.* **7**, 225–233 (2024).
- Zhang, W. et al. Neuro-inspired computing chips. *Nat. Electron.* **3**, 371–382 (2020).
- Roy, K., Jaiswal, A. & Panda, P. Towards spike-based machine intelligence with neuromorphic computing. *Nature* **575**, 607–617 (2019).
- Wu, G. et al. Ferroelectric-defined reconfigurable homojunctions for in-memory sensing and computing. *Nat. Mater.* **22**, 1499–1506 (2023).
- Tang, X., Shen, H., Zhao, S., Li, N. & Liu, J. Flexible brain-computer interfaces. *Nat. Electron.* **6**, 109–118 (2023).
- Zhang, H.-S. et al. Co-assembled perylene/graphene oxide photo-sensitive heterobilayer for efficient neuromorphics. *Nat. Commun.* **13**, 4996 (2022).
- Jiang, T. et al. Tetrachromatic vision-inspired neuromorphic sensors with ultraweak ultraviolet detection. *Nat. Commun.* **14**, 2281 (2023).
- Wang, X. et al. Enhanced multiwavelength response of flexible synaptic transistors for human sunburned skin simulation and neuromorphic computation. *Adv. Mater.* **35**, 202303699 (2023).
- Zhu, X. et al. High-contrast bidirectional optoelectronic synapses based on 2D molecular crystal heterojunctions for motion detection. *Adv. Mater.* **35**, 202301468 (2023).
- Chen, K. et al. Organic optoelectronic synapse based on photon-modulated electrochemical doping. *Nat. Photonics* **17**, 629–637 (2023).
- Wu, X. et al. Wearable in-sensor reservoir computing using optoelectronic polymers with through-space charge-transport characteristics for multi-task learning. *Nat. Commun.* **14**, 468 (2023).
- Liu, S. et al. An ultrasmall organic synapse for neuromorphic computing. *Nat. Commun.* **14**, 7655 (2023).
- Medina, I. et al. Reflection of near-infrared light confers thermal protection in birds. *Nat. Commun.* **9**, 3610 (2018).
- Gu, L. et al. A biomimetic eye with a hemispherical perovskite nanowire array retina. *Nature* **581**, 278–282 (2020).
- Tedore, C. & Nilsson, D. E. Avian UV vision enhances leaf surface contrasts in forest environments. *Nat. Commun.* **10**, 238 (2019).
- Matthew, B. T. et al. Complementary shifts in photoreceptor spectral tuning unlock the full adaptive potential of ultraviolet vision in birds. *eLife* **5**, e15675 (2016).
- Wang, C.-Y. et al. Gate-tunable van der Waals heterostructure for reconfigurable neural network vision sensor. *Sci. Adv.* **6**, eaba6173 (2020).
- Han, N. et al. GaAs nanowires: from manipulation of defect formation to controllable electronic transport properties. *ACS. Nano* **7**, 9138–9146 (2013).
- Bai, L., Wang, N. & Li, Y. Controlled growth and self-assembly of multiscale organic semiconductor. *Adv. Mater.* **34**, 2102811 (2022).
- Chen, Z. et al. Organic semiconductor crystal engineering for high-resolution layer-controlled 2D crystal arrays. *Adv. Mater.* **34**, 2104166 (2022).
- Liao, F. et al. Bioinspired in-sensor visual adaptation for accurate perception. *Nat. Electron.* **5**, 84–91 (2022).
- Du, Y. et al. One-dimensional van der Waals material tellurium: Raman spectroscopy under strain and magneto-transport. *Nano. Lett.* **17**, 3965–3973 (2017).
- Zhou, K.-G. et al. Raman modes of MoS₂ used as fingerprint of van der Waals interactions in 2-D crystal-based heterostructures. *ACS. Nano* **8**, 9914–9924 (2014).
- Irwin, M. D. et al. P-Type semiconducting nickel oxide as an efficiency-enhancing anode interfacial layer in polymer bulk-heterojunction solar cells. *Proc. Natl Acad. Sci. USA* **105**, 2783–2787 (2008).
- Chen, X. et al. Gate-tunable the interface properties of GaAs-WSe₂ (1D-2D) vdWs heterojunction for high-responsivity, self-powered photodetector. *Appl. Phys. Lett.* **118**, 041102 (2021).
- Gauthier, D. J., Bollt, E., Griffith, A. & Barbosa, W. A. S. Next generation reservoir computing. *Nat. Commun.* **12**, 5564 (2021).
- Yu, X.-X. et al. Piezo-phototronic effect modulated self-powered UV/visible/near-infrared photodetectors based on CdS:P3HT microwires. *Nano. Energy* **34**, 155–163 (2017).
- Park, S. H. et al. 3D printed polymer photodetectors. *Adv. Mater.* **30**, 1803980 (2018).
- Fang, F. et al. Two-dimensional Cs₂AgBiBr₆/WS₂ heterostructure-based photodetector with boosted detectivity via interfacial engineering. *ACS. Nano* **16**, 3985–3993 (2022).
- Yang, S. et al. Van der Waals epitaxy of Bi₂Te₂Se/Bi₂O₂Se vertical heterojunction for high performance photodetector. *Small* **18**, 2105211 (2021).
- Gou, G. et al. High-performance and flexible photodetectors based on P3HT/CdS/CdS:SnS₂ superlattice nanowires hybrid films. *Appl. Phys. A* **123**, 731 (2017).
- Zhang, Z. et al. All-in-one two-dimensional retinomorphic hardware device for motion detection and recognition. *Nat. Nanotechnol.* **17**, 27–32 (2022).
- Zhu, X. et al. Enhancing performance of a GaAs/AlGaAs/GaAs nanowire photodetector based on the two-dimensional electron-hole tube structure. *Nano. Lett.* **20**, 2654–2659 (2020).
- Zhu, X. et al. Negative phototransistors with ultrahigh sensitivity and weak-light detection based on 1D/2D molecular crystal p–n heterojunctions and their application in light encoders. *Adv. Mater.* **34**, 2201364 (2022).
- Jin, C. et al. Artificial vision adaption mimicked by an optoelectrical In₂O₃ transistor array. *Nano. Lett.* **22**, 3372–3379 (2022).

38. Shi, Q. et al. Progress in wearable electronics/photronics-moving toward the era of artificial intelligence and internet of things. *Info-Mat* **2**, 1131–1162 (2020).
39. Son, S. Y. et al. Integrating charge mobility, stability and stretchability within conjugated polymer films for stretchable multifunctional sensors. *Nat. Commun.* **13**, 2739 (2022).
40. Kim, D. C., Shim, H. J., Lee, W., Koo, J. H. & Kim, D.-H. Material-based approaches for the fabrication of stretchable electronics. *Adv. Mater.* **32**, 1902743 (2020).
41. Park, S., Cho, K., Oh, H. & Kim, S. Electrical and mechanical characteristics of fully transparent IZO thin-film transistors on stress-relieving bendable substrates. *Appl. Phys. Lett.* **109**, 143504 (2016).
42. Noguchi, Y. et al. Pressure modulation of backbone conformation and intermolecular distance of conjugated polymers toward understanding the dynamism of π -figuration of their conjugated system. *J. Phys. Chem. B* **119**, 7219–7230 (2015).
43. Tsoi, W. C. et al. The nature of in-plane skeleton Raman modes of P3HT and their correlation to the degree of molecular order in P3HT: PCBM blend thin films. *J. Am. Chem. Soc.* **133**, 9834–9843 (2011).
44. Skrypnichuk, V. et al. Enhanced vertical charge transport in a semiconducting P3HT thin film on single layer graphene. *Adv. Funct. Mater.* **25**, 664–670 (2015).
45. Shen, X., Duzhko, V. V. & Russell, T. P. A study on the correlation between structure and hole transport in semi-crystalline regioregular P3HT. *Adv. Energy Mater.* **3**, 263–270 (2013).
46. Treat, N. D. et al. Interdiffusion of PCBM and P3HT reveals miscibility in a photovoltaically active blend. *Adv. Energy Mater.* **1**, 82–89 (2011).
47. Noori, K. & Giustino, F. Ideal energy-level alignment at the ZnO/P3HT photovoltaic interface. *Adv. Funct. Mater.* **22**, 5089–5095 (2012).
48. Tsai, M.-Y. et al. A reconfigurable transistor and memory based on a two-dimensional heterostructure and photoinduced trapping. *Nat. Electron.* **6**, 755–764 (2023).
49. Khan, M. U., Abbas, Y., Rezeq, M. D., Alazzam, A. & Mohammad, B. Unidirectional neuromorphic resistive memory integrated with piezoelectric nanogenerator for self-power electronics. *Adv. Funct. Mater.* **34**, 2305869 (2023).
50. Lee, Y., Park, H.-L., Kim, Y. & Lee, T.-W. Organic electronic synapses with low energy consumption. *Joule* **5**, 794–810 (2021).
51. Su, W. et al. Interlayer transition induced infrared response in ReS₂/2D perovskite van der Waals heterostructure photodetector. *Nano. Lett.* **22**, 10192–10199 (2022).
52. Zhao, Y. et al. Modification of C₆₀ nano-interlayers on organic field-effect transistors based on 2,7-diocetyl[1]benzothieno-[3,2-b]benzothiophene (C8-BTBT)/SiO₂. *Results Phys.* **19**, 103590 (2020).
53. Du, C. et al. Reservoir computing using dynamic memristors for temporal information processing. *Nat. Commun.* **8**, 2204 (2017).
54. Hong, S. et al. Highly sensitive active pixel image sensor array driven by large-area bilayer MoS₂ transistor circuitry. *Nat. Commun.* **12**, 3559 (2021).
55. Zhang, Z. et al. In-sensor reservoir computing system for latent fingerprint recognition with deep ultraviolet photo-synapses and memristor array. *Nat. Commun.* **13**, 6590 (2022).
56. Wang, X. et al. Vertically integrated spiking cone photoreceptor arrays for color perception. *Nat. Commun.* **14**, 3444 (2023).
57. Xu, Y. et al. Flexible multiterminal photoelectronic neurotransmitters based on self-assembled rubber semiconductors for spatiotemporal information processing. *SmartMat* **4**, e1162 (2023).
58. Hou, J. J. et al. Synthesis and characterizations of ternary InGaAs nanowires by a two-step growth method for high-performance electronic devices. *ACS Nano* **6**, 3624–3630 (2012).
59. Fan, Z. et al. Wafer-scale assembly of highly ordered semiconductor nanowire arrays by contact printing. *Nano. Lett.* **8**, 20–25 (2008).
60. Takahashi, T. et al. Monolayer resist for patterned contact printing of aligned nanowire arrays. *J. Am. Chem. Soc.* **131**, 2102–2103 (2009).

Acknowledgements

We acknowledge a fellowship award from the Research Grants Council of the Hong Kong Special Administrative Region, China (CityU RFS2021–1S04) and the Innovation and Technology Fund (MHP/126/21) from the Innovation and Technology Commission of the Government of the Hong Kong Special Administrative Region of the People's Republic of China. J.C.H. and J.S. acknowledge the support from the National Key Research and Development Program of China (No. 2023YFE0208600).

Author contributions

P.X., Y.X., J.W., and J.C.H. structured and designed the experiments. P.X., Y.X. performed the fabrication and characterization of thin films and devices. J.W. finished the simulation of the devices. D.L., Y.Z., Z.Z., B.L., Y.Y., Y.L., and W.W. helped with photoelectric performance measurements. P.X., Y.X., Y.M., J.C.H., B.G., Q.Q., Y.S., and J.S. analyzed the data. P.X., Y.X., J.W., and J.C.H. co-wrote the paper. All authors discussed the results and commented on the manuscript.

Competing interests

The authors declare no competing interest.

Additional information

Supplementary information The online version contains supplementary material available at <https://doi.org/10.1038/s41467-024-52563-4>.

Correspondence and requests for materials should be addressed to Jia Sun or Johnny C. Ho.

Peer review information *Nature Communications* thanks Yen-Fu Lin, and the other, anonymous, reviewer(s) for their contribution to the peer review of this work. A peer review file is available.

Reprints and permissions information is available at <http://www.nature.com/reprints>

Publisher's note Springer Nature remains neutral with regard to jurisdictional claims in published maps and institutional affiliations.

Open Access This article is licensed under a Creative Commons Attribution-NonCommercial-NoDerivatives 4.0 International License, which permits any non-commercial use, sharing, distribution and reproduction in any medium or format, as long as you give appropriate credit to the original author(s) and the source, provide a link to the Creative Commons licence, and indicate if you modified the licensed material. You do not have permission under this licence to share adapted material derived from this article or parts of it. The images or other third party material in this article are included in the article's Creative Commons licence, unless indicated otherwise in a credit line to the material. If material is not included in the article's Creative Commons licence and your intended use is not permitted by statutory regulation or exceeds the permitted use, you will need to obtain permission directly from the copyright holder. To view a copy of this licence, visit <http://creativecommons.org/licenses/by-nc-nd/4.0/>.

© The Author(s) 2024